Article

Assessing the Accuracy of ALOS/PALSAR-2 and Sentinel-1 Radar Images in Estimating the Land Subsidence of Coastal Areas: A Case Study in Alexandria City, Egypt

Noura Darwish [1], Mona Kaiser [1], Magaly Koch [2] and Ahmed Gaber [3,*]

1   Geology Department, Faculty of Science, Suez Canal University, Ismailia 41522, Egypt; nourahmoustafa123@yahoo.com (N.D.); mona_kaysar@science.suez.edu.eg (M.K.)
2   Center for Remote Sensing, Boston University, Boston, MA 02215, USA; Mkoch@bu.edu
3   Geology Department, Faculty of Science, Port Said University, Port Said 42522, Egypt
*   Correspondence: gaber@sci.psu.edu.eg

Abstract: Recently, the Differential Interferometric Synthetic Aperture Radar (DInSAR) technique is widely used for quantifying the land surface deformation, which is very important to assess the potential impact on social and economic activities. Radar satellites operate in different wavelengths and each provides different levels of vertical displacement accuracy. In this study, the accuracies of Sentinel-1 (C-band) and ALOS/PALSAR-2 (L-band) were investigated in terms of estimating the land subsidence rate along the study area of Alexandria City, Egypt. A total of nine Sentinel-1 and 11 ALOS/PALSAR-2 scenes were used for such assessment. The small baseline subset (SBAS) processing scheme, which detects the land deformation with a high spatial and temporal coverage, was performed. The results show that the threshold coherence values of the generated interferograms from ALOS-2 data are highly concentrated between 0.2 and 0.3, while a higher threshold value of 0.4 shows no coherent pixels for about 80% of Alexandria's urban area. However, the coherence values of Sentinel-1 interferograms ranged between 0.3 and 1, with most of the urban area in Alexandria showing coherent pixels at a 0.4 value. In addition, both data types produced different residual topography values of almost 0 m with a standard deviation of 13.5 m for Sentinel-1 and −20.5 m with a standard deviation of 33.24 m for ALOS-2 using the same digital elevation model (DEM) and wavelet number. Consequently, the final deformation was estimated using high coherent pixels with a threshold of 0.4 for Sentinel-1, which is comparable to a threshold of about 0.8 when using ALOS-2 data. The cumulative vertical displacement along the study area from 2017 to 2020 reached −60 mm with an average of −12.5 mm and mean displacement rate of −1.73 mm/year. Accordingly, the Alexandrian coastal plain and city center are found to be relatively stable, with land subsidence rates ranging from 0 to −5 mm/year. The maximum subsidence rate reached −20 mm/year and was found along the boundary of Mariout Lakes and former Abu Qir Lagoon. Finally, the affected buildings recorded during the field survey were plotted on the final land subsidence maps and show high consistency with the DInSAR results. For future developmental urban plans in Alexandria City, it is recommended to expand towards the western desert fringes instead of the south where the present-day ground lies on top of the former wetland areas.

Keywords: Sentinel-1; ALOS/PALSAR-2; land subsidence; accuracy assessment; Alexandria City; Egypt

1. Introduction

Coastal cities along the Nile Delta encompass most of the social and economic activities in Egypt. Meanwhile, the combined impact of sea level rise and land subsidence causes serious risks and problems [1]. Together, subsidence and lack of sediment supply along the depositional zone of the Nile Basin (downstream Nile Delta) caused by the intensive construction of dams could potentially cause a relative rise in sea level over time [2]. Additionally, coastal erosion is predicted to increase hazard risks in coastal cities [3,4]. Therefore,

there is an urgent need for regular monitoring, with high accuracy, the deformation in coastal cities in order to mitigate the expected hazards. Traditional survey instruments are point observations and thus have a spatially limited coverage. Remote sensing techniques are more cost-effective and provide better spatial coverage for coastal and land observations [5–11].

Numerous studies have been conducted to measure land subsidence in coastal areas across the Nile Delta of Egypt using SAR remote sensing data [12–25]. Information on the spatial distribution of natural hazards needs to be generated as quickly as possible in order to be useful for emergency response efforts [26]. Such information is usually generated from the analysis of optical satellite imagery [27,28]. However, relying only on optical satellite imagery for natural hazards assessment is problematic as the mapping processes can be significantly delayed by cloud cover and bad weather conditions [29]. Synthetic Aperture Radar (SAR) satellite imagery provides an alternative method to generate information under all-weather conditions. SAR is most widely used to measure the downslope velocity of slow-moving landslides and to provide subtle measurements of coastal subsidence at a significantly improved spatial resolution and over large areas [30–41].

Achache et al. 1996 [42] have demonstrated the ability of InSAR to monitor small displacements at the required scale for large landslide monitoring and their work shows similar trends to those acquired from ground-based measurements. Many studies are adopting InSAR technology for land subsidence tracking, and the derived patterns and results are comparable to ground-based measurements [43–46]. In this context, high-accuracy monitoring methods, including persistent scatterer InSAR [47] and small baseline subset DInSAR (SBAS-InSAR) [48], were proposed and applied to monitor land subsidence with high accuracy. Indeed, the SBAS approach allows for the detection of land deformation at high spatial and temporal coverage. This research work aims to improve the SBAS DInSAR methodology and to determine the best SAR data (L-band or C-band) for estimating the land-subsidence rate with high accuracy in an economically important and densely populated part of the Nile Delta of Egypt, which has suffered from many subsidence events in recent years [49]. In addition, a systematic comparison of two SAR sensors (ALOS/PALSAR-2 and Sentinel-1A) is presented to determine which dataset provided the most suitable and accurate results of land subsidence measure in locations showing high coherence within the Alexandrian urban area (Figure 1).
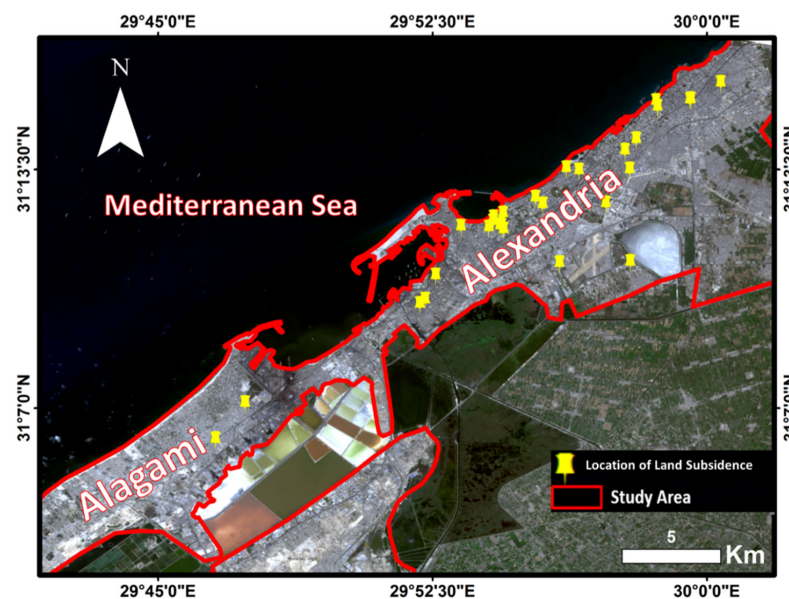

Figure 1. The urban study area in Alexandria City is outlined with a red border plotted on a Sentinel-2 image of October 2019. The yellow dots represent the recently recorded subsidence events.

2. Study Area

Alexandria was chosen as a research area due to its complicated pattern of urban subsidence. The city lies on the Mediterranean Sea at the western edge of the Nile Delta, about 183 km northwest of Cairo City and encloses an area of approximately 2679 km^2. It is Egypt's second-largest city and a major economic center. It hosts 40% of the Egyptian industrial and commercial activities, as well as the largest harbor in the country [50,51]. It is located in a moderately tectonically stable plate in North East Africa. The periodic instability has been caused by the readjustment to downwrapping (sediment compaction, faulting, isostatic lowering) of the sedimentary sequences (locally exceeding 4000 m) [52,53].

Generally, the low-lying region of the Nile Delta is subjected to significant differential subsidence. The reduction in annual Nile water and sediment discharge over the last two centuries associated with dams constructions along the Nile River has resulted in an environmental imbalance along the depositional zone of the Nile watershed, and thus, has increased the impact of sea level rise across the city [54].

Many subsidence events were recorded along Alexandria City in recent years [49]. Land subsidence in Alexandria has not been thoroughly documented in the literature; however, subsidence was partially studied using traditional geological measurements, mostly in the eastern and southern parts of the city [55,56]. The DInSAR technique has been used to study land subsidence in the central part of the city and its relation to sea level rise [57]. It is worth mentioning that the previous DInSAR studies in Alexandria mainly focused on the period before 2015, using a variety of radar images with different wavelengths and producing results with different levels of accuracy.

3. Datasets

In this study, a total of 11 ALOS/PALSAR-2 L-band images acquired from 8 March 2015 to 31 March 2019, as well as 9 Sentinel-1A C-band images acquired from 7 August 2017 to 24 January 2020 were utilized to map the ground deformation over Alexandria City, Egypt. The ALOS-2 acquisitions were captured in ScanSAR mode, ascending with single-look complex format (SLC), right-looking and HH polarization. All the Sentinel-1 images were acquired in the descending path, SLC format and Interferometric Wide (IW) swath mode. The short sampling rate of the Sentinel-1 images has the potential to maintain the coherence, even if the wavelength is short (~5.5 cm). The ALOS-2 images with a longer wavelength (~24 cm) are less affected by temporal decorrelation of the SAR signal. Table 1 lists the details of the used SAR data.

Table 1. Characteristics of ALOS/PALSAR-2 and Sentinel-1A SAR data used in this study.

Satellite	ALOS/PALSAR-2	Sentinel-1A
Band	L	C
Orbit	Ascending	Descending
Master image	27 November 2016	27 June 2018
Number of scenes	11	9
Acquisition period	2015–2019	2017–2020
λ (cm)	23.6	5.6
Polarization	HH	VV
Revisit cycle	14 days	12 days
Mode	ScanSAR	IW

Sentinel-1 products consist of three main sub-swaths (Figure 2, red labels) for each polarization channel, with a total of three (single polarizations) or six (dual polarization) images in an IW product. Each sub-swath image consists of a number of bursts (Figure 2, white labels), where each burst has been processed as a separate SLC image. The individually focused complex burst images are combined, in azimuth-time order, into a single sub-swath image with black-fill demarcation in between. The data used in evaluating the

land subsidence in Alexandria City lies in the sub-swath IW2 in the western part of Nile Delta.
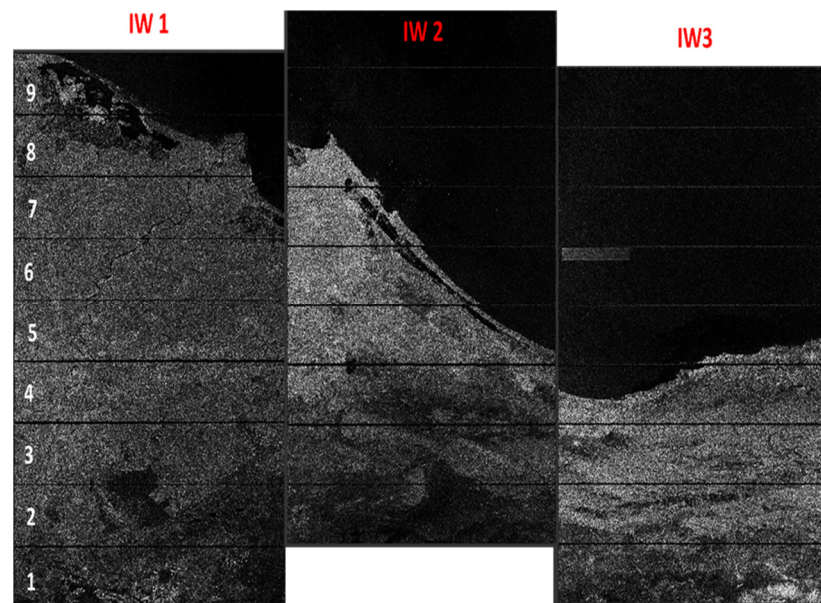

Figure 2. Sub-swaths (red) and bursts (white) of Sentinel-1 products of the study area.

4. SBAS Processing

The Interferometric analysis of ALOS/PALSAR-2 and Sentinel-1A sensors was carried out through the SBAS method [58]. All acquired steps to calculate the rates of displacement affecting the study area are shown in Figure 3. Firstly, the specifications of the perpendicular and temporal baselines thresholds for processing were calculated based on the conditions of the study area and the used SAR data. If the study area is urban, the time baseline can be set for a longer period, as several stable points can stay without changing their coherence over a long time period. An interferogram can still be generated over an urban area, even if the temporal baseline is up to four years [59]. Based on these considerations, the connection graphs were produced for each group (Figure 4). A comparison was made between the spatial and temporal baselines of the radar images. Subsequently, the links between radar images were built to show which baselines are small enough to be comparable [60].

The result is a network of connections, defined as a connection graph (Figure 4a,b), where the yellow and green dots in these graphs represent the super master and the slave of the SAR images, respectively. The red lines represent the interferograms that pass the SBAS minimal requirements. Figure 4c,d indicate the distance between the various images, depending on the date of acquisition. These graphs make it possible to conduct a quick visual evaluation of the relations between the images and the time distribution of the SAR data being used. Consequently, pairs of images were generated and later used to create interferograms [61,62]. For the ALOS/PALSAR-2 data (2015–2019) about 39 pairs of interferograms were generated and 22 pairs for Sentinel-1A data (2017–2020).

Each pair of compatible radar images identified in the previous step is used to generate an interferogram. In addition to the radar images and the connecting graph, this process requires the use of an accurate digital terrain model [61]. The digital elevation model SRTM 1-arcsecond provided by NASA with a resolution of 30 m was used in this study. During the first step of co-registration, all SAR images were geometrically adjusted by resampling each image with the master, which was chosen during the correlation step to give them the same geometry [62,63]. During the second stage, a stack of interferograms formed, followed by a process of flattening.
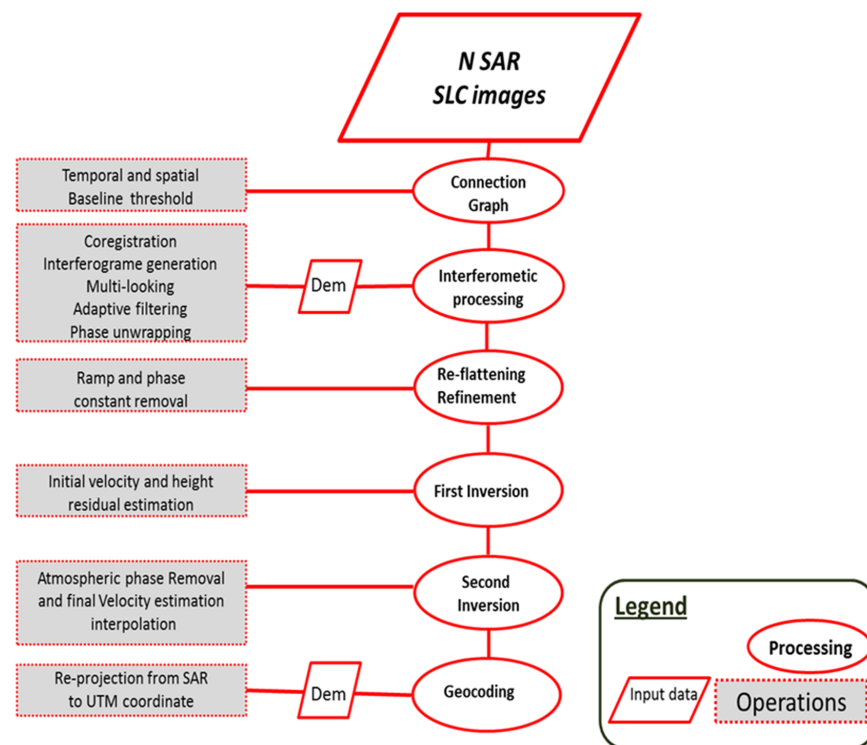
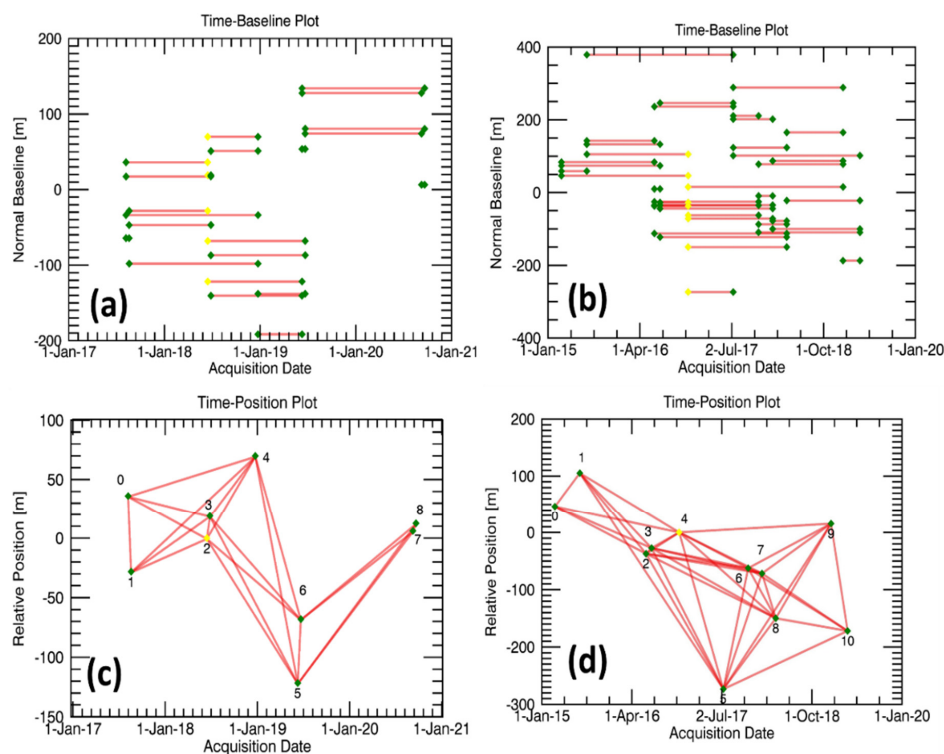**Figure 3.** Flowchart of SBAS-DInSAR processing steps.

Figure 4. The temporal and spatial baseline distributions of the SAR interferograms from the Sentinel-1A and ALOS/PALSAR-2 data sets (**a**–**d**), where each acquisition is represented by a diamond associated to an ID number; the green diamonds represent the valid acquisitions and the yellow diamonds represent the super master image of the small baseline subset (SBAS). (**a**) Time–baseline plot of SBAS interferograms generated by the Sentinel-1A data, with 27 June 2018 as the super master image (**b**) time–baseline plot of SBAS interferograms generated by the ALOS/PALSAR-2 data, with 27 November 2016 as the super master image; (**c**) time–position plot generated by the Sentinel-1A and (**d**) time–position plot generated by the ALOS/PALSAR-2.

In this study, the multi-looking process was performed by setting the number of looks for both SAR data (ALOS/PALSAR-2 and Sentinel-1A) as 1 in the range direction and 4 in azimuth direction. Such multi-looking process increases Signal to Noise Ratio (SNR) of the interferograms and thus improves the quality of coherence estimation [64]. Next, interferograms were generated after meeting the temporal, geometric baseline and Doppler difference criteria. The formed interferograms are considered as Stripmap like interferograms, thus phase filtering and unwrapping were implemented. There are several methods for unwrapping the interferograms; however, in this study, the Minimum Cost Flow (MCF) method was used for both ALOS/PALSAR-2 and Sentinel-1A data. The other methods were tested, compared visually, and were found to be less suited for the study area than the MCF method.

In order to use the possible maximum number of coherent pixels a compromise value of 0.35 is suggested, when using the minimum cost flow method for the unwrapping stage. Indeed, all areas with coherence lower than the 0.35 threshold value were eliminated. As low coherence values can lead to particularly noisy areas in the analysis, it reduces the reliability of the final results [65]. Besides unwrapping interferograms, coherence maps for each interferogram were generated. Therefore, the Goldstein filters were applied to the generated interferograms in order to minimize the amount of noise [66].

In order to re-flatten the interferograms, ground control points (GCPs) are required as input, which should be positioned on areas that are thought to be stable or with pre-known deformation values. The height values of these GCPs were estimated from the input DEM [67]. In this study a total number of 150 points were used and manually placed only on the persistent scatterers with very high coherence pixels to ensure that each interferogram has received the necessary amount of control points to correct any inconsistencies caused by orbital fluctuations and re-flattening the interferograms to make phase data more accurate [68].

Following the previous processing scheme, the first inversion step was applied to the generated and re-flattened interferograms in order to measure the residual height and the velocity of the displacement using the linear model [69]. In the same context, the second unwrapping process was performed to improve the SAR data for the next step. In addition, the second inversion step was applied to provide more accurate estimation of the final velocity displacement. The high and low pass atmospheric filter was applied to remove the noise through temporal and spatial filtering operations [70,71]. The displacement observed by DInSAR is one dimensional along the Line of Sight (LOS). In order to convert the LOS displacement to the vertical direction (subsidence), an additional equation was used [72]. This operation suggests that the displacement is primarily caused by the subsidence (vertical displacement) and that the horizontal displacement, which is in the same direction of the LOS is very small compared to the vertical subsidence; thus, it can be ignored. However, it is very difficult to convert the measured phase change along the LOS into the perpendicular horizontal displacement. Therefore, the geocoding was applied to the different outputs from the previous steps to convert the slant range format to the geocoded images with the required coordinate system. Finally, the data was exported in the Geotiff format to ArcGIS, where statistics have been calculated.

5. Results

After assessing the accuracy of both ALOS-2 and Sentinel-1 in estimating the vertical displacement, the final land subsidence rate of Alexandria City and its surroundings was monitored from August 2017 to September 2020 by using nine Sentinel-1 SAR images with 5×20 m spatial resolution and VV polarization. A total of 22 interferometric pairs were generated using the image of 27 June 2018 as the super master. All slant ranges of the nine images were co-registered with this super master, which was used as the reference image.

Selecting the proper perpendicular and temporal baselines is considered to be a very important step to discard the unsuitable SAR images and to examine the validity of the generated interferograms. For Sentinel-1 interferograms, the mean absolute normal

baseline was 78 m with minimum and maximum absolute baseline of 13 m and 191 m, respectively. The mean absolute temporal baseline was 285 days with minimum and maximum value equal to 12 days and 504 days, respectively. Table 2 illustrates each master and slave image of Sentinel-1, which was combined to generate 22 interferograms. While, for ALOS/PALSAR-2 interferograms, the mean absolute normal baseline was 110 m with minimum and maximum absolute baseline of 18 m and 287 m, respectively. The mean absolute temporal baseline was 329 days with minimum and maximum values equal to 28 days and 600 days, respectively.
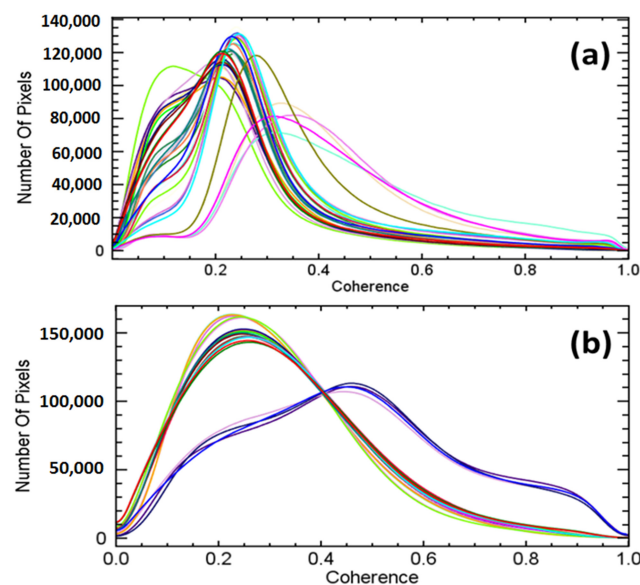
Table 2. Sentinel-1 data pairs for SBAS processing.

Master	Slave	Normal Baseline (m)	Temporal Baseline (Days)
7/8/2017	19/8/2017	−62	12
	15/6/2018	−36	312
	27/6/2018	−20	324
	24/12/2018	34	504
19/8/2017	15/6/2018	28	300
	26/6/2018	44	312
	24/12/2018	95	492
15/6/2018	27/6/2018	18	12
	24/12/2018	69	192
	10/6/2019	−121	360
	22/6/2019	−68	372
27/6/2018	28/12/2018	53	180
	10/6/2019	−138	348
	22/6/2019	−84	360
24/12/2018	22/6/2019	−191	168
	10/6/2019	−138	180
10/6/2019	22/6/2019	54	12
	8/9/2020	126	456
	20/9/2020	134	468
22/6/2019	8/9/2020	72	444
	20/9/2020	80	456
8/9/2020	20/9/2020	13	12

Table 3 illustrates the temporal and normal baseline for each master and slave ALOS/PALSAR-2 interferogram pairs, which were combined to generate 33 interferograms. The mean absolute value of the normal and absolute baseline for ALOS-2 interferograms is higher than the value of Sentinel-1 interferograms, with approximately 32 m and 44 days, respectively. The increase in baselines has a negative effect on the reliability and accuracy of the generated interferograms. The correlation between the pixels of the used SAR pair in terms of power and phase is recognized as coherence. The zero coherence means there is no matching between the pixels with high changes on the ground and coherence value of 1 means complete matching with no change. The coherence decreases due to an increase in the normal and temporal baseline, as well as in situ anthropogenic activities. Figure 5 illustrates the coherence values of the generated interferograms from Sentinel-1 and ALOS-2 data. The histograms in Figure 5a show the coherence of ALOS-2 interferograms, with values concentrating mostly in the range between 0.2 and 0.3. Whereas, Figure 5b represents the coherence value of Sentinel-1 interferograms, with values ranging between 0.3 and 1. Based on these histograms and the distribution of coherence values, the coherence thresholds were selected as 2 and 4 for ALOS/PALSAR-2 and Sentinel-1A, respectively.

Table 3. ALOS/PALSAR-2 data pairs for SBAS processing.

Master	Slave	Normal Baseline (m)	Temporal Baseline (Days)
8/3/2015	12/7/2015	84	126
	12/6/2016	−56	462
	10/7/2016	−34	490
12/7/2015	12/6/2016	−134	336
	10/7/2016	−111	364
	27/11/2016	−105	504
12/6/2016	10/7/2016	22	28
	27/11/2016	37	168
	9/7/2017	−242	392
	12/11/2017	−35	518
	21/1/2018	−36	588
10/7/2016	21/1/2018	−58	560
	12/11/2017	−57	490
	9/7/2017	−264	384
	27/11/2016	27	140
27/11/2016	1/4/2018	−149	490
	21/1/2018	−71	420
	12/11/2017	−62	350
	9/7/2017	−273	224
9/7/2017	6/1/2019	287	546
	1/4/2018	128	266
	21/1/2018	206	196
	12/11/2017	211	126
12/11/2017	31/3/2019	−109	504
	6/1/2019	76	420
	1/4/2018	−87	140
	21/1/2018	−18	70
21/10/2018	31/3/2019	−102	434
	6/1/2019	83	390
1/4/2018	1/4/2018	134	468
	6/1/2019	−79	70
	31/3/2019	−23	364
6/1/2019	31/3/2019	−185	84

Figure 5. Illustrates the coherence values distribution of interferograms produced from the ALOS-2 data (**a**) and coherent interferogram values produced from the Sentinel-1 data (**b**).

The generated interferograms, which show strong residual phase ramps and jumps originated from the orbital inaccuracies, together with large atmospheric artifacts, were corrected by removing the residual phase frequency. Since Alexandria City lies in a coastal area with a dense cloud cover during the winter season, the atmospheric artifact was expected to cause a negative effect on the interferograms quality. The very large temporal or normal baseline between the two acquisitions resulted in the generation of wrapped interferograms with very low coherence; thus, these interferograms were discarded (Figure 6).
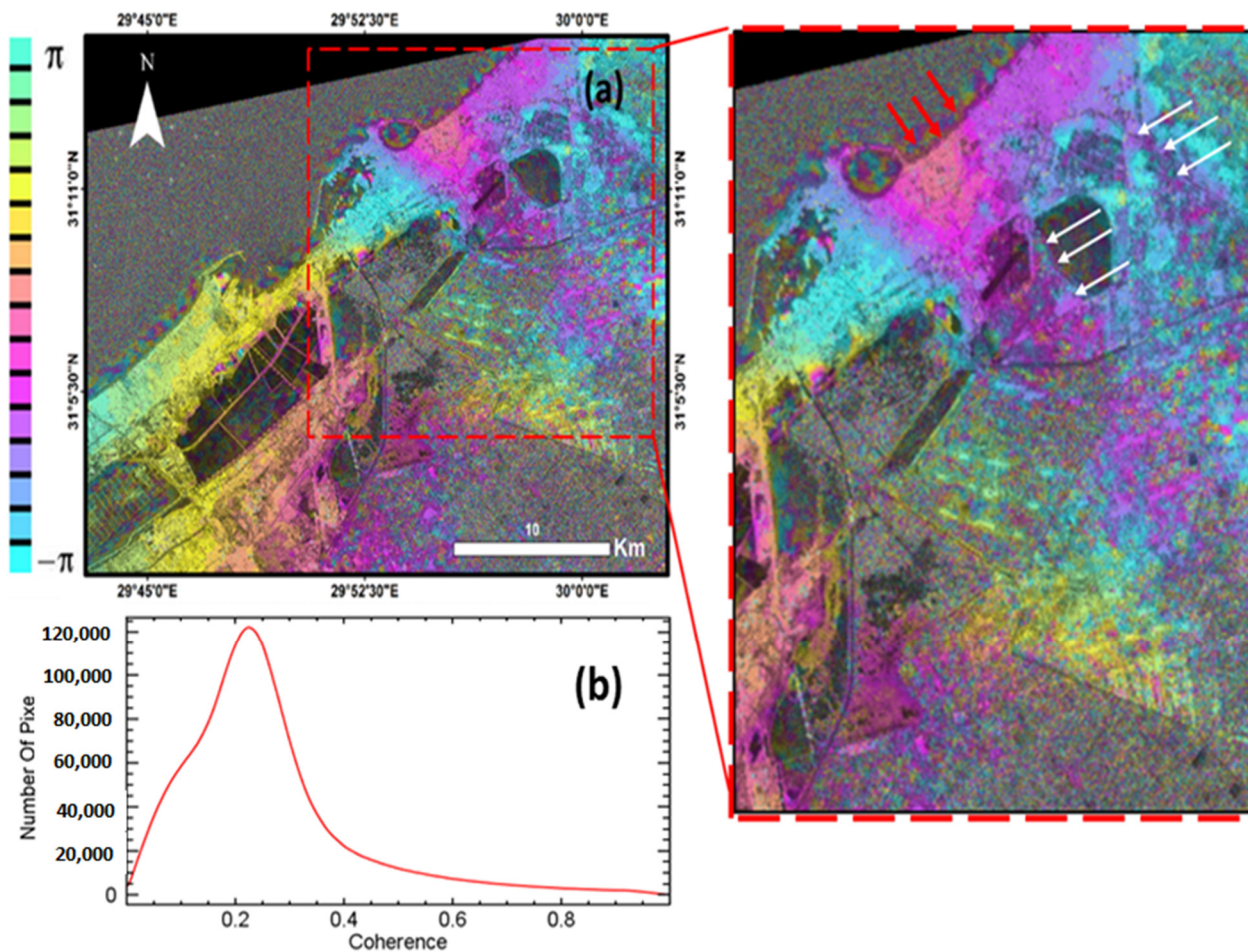

Figure 6. (**a**) Wrapped ALOS-2 low coherent interferogram showing errors during the flattening sub-step; white arrow indicates systematic residual fringes that could have been caused by strong orbital inaccuracy or issues with some parameter settings, while red arrows indicate strong atmospheric artifacts and phase jumps. (**b**) Histogram representing the coherence value of interferogram with a mean coherent value of 0.15.

However, the highest coherent Sentinel-1 wrapped interferogram (Master 15 December 2018 and Slave 10 June 2019) was considered to be acceptable. The urban areas have shown high coherent pixels without any phase jump, unlike the agricultural cover, which shows low coherent pixels (Figure 7). Wrapped interferograms were subsequently filtered and used together with the coherence data to calculate the phase unwrapping. The unwrapped interferogram were refined and re-flattened by using the residual phase method to estimate and remove the remaining phase constants and phase ramps, in order to relate the change in slant range to the deformation only (due to subsidence). A total of 150 GCPs were selected for both Sentinel-1 and ALOS-2 data, where the unwrapped phase value was close to zero and the flat areas were identified.
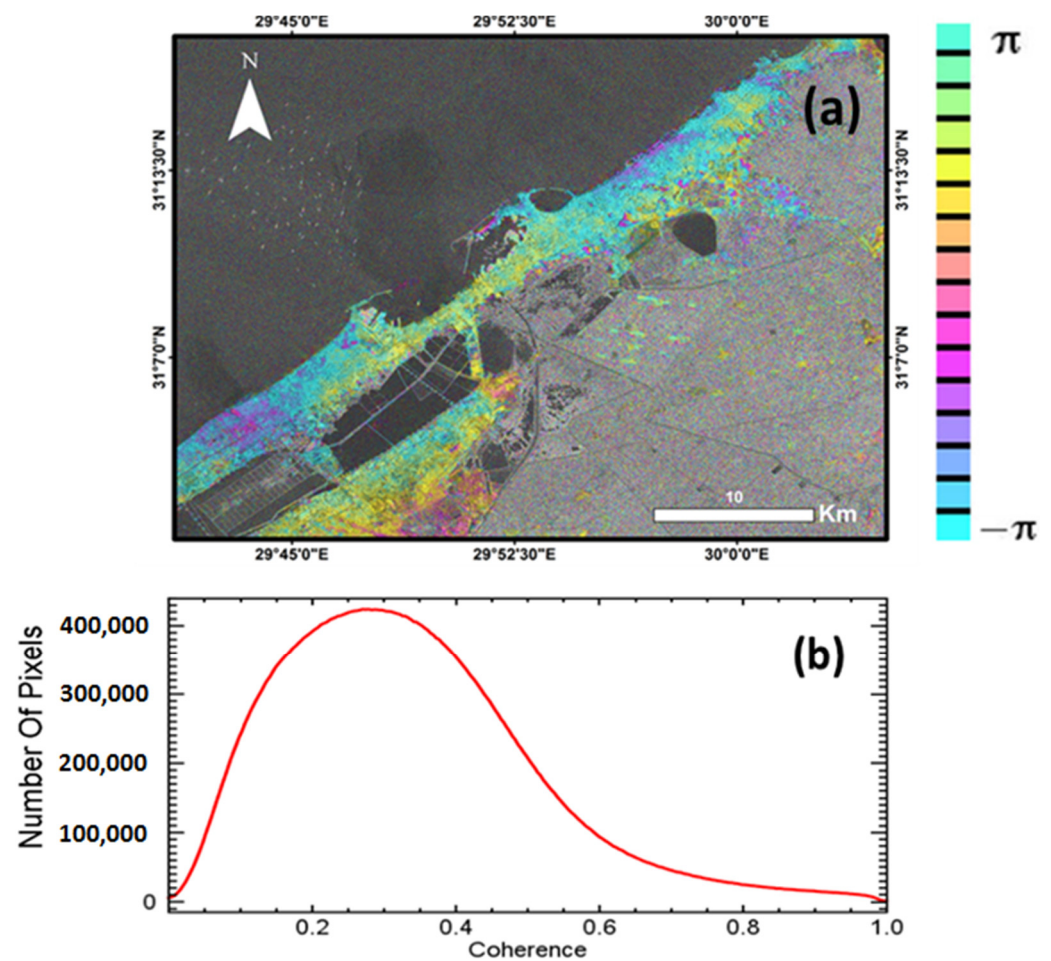
Figure 7. Wrapped Sentinel-1 interferogram with low coherence. The cause is the very large temporal and normal baseline between the two acquisitions used to make the interferogram (**a**). The histogram illustrates the coherence value between two interferogram pairs (master 15 December 2018 and Slave 10 June 2019) (**b**).

The linear model was used to estimate the residual height and the displacement velocity [73]. An incorrect residual topography calculation will cause horizontal shifts in the final SBAS geocoding results. The accuracy of the residual topography calculation depends on the vertical and horizontal accuracy of the used DEM, as well as the pixel spacing of SAR data [73,74]. In this study, the freely available SRTM data was used for estimating the residual topography. But due to the high spatial resolution of Sentinel-1 interferograms, its sensitivity is large enough to estimate the average residual topography to almost 0 m with a standard deviation equal to 13.5 m using 1 as a wavelet number (Figure 8c). Moreover, the accuracy of the ALOS-2 interferograms was also checked using the same SRTM data and the same wavelet number and showed average residual topography equal to −100 m and high standard deviation equal to 70 m (Figure 8a). Meanwhile, by using two wavelet numbers, the ALOS-2 interferograms showed average residual topography equal to −20.5 m and standard deviation equal to 33.24 m (Figure 8b).
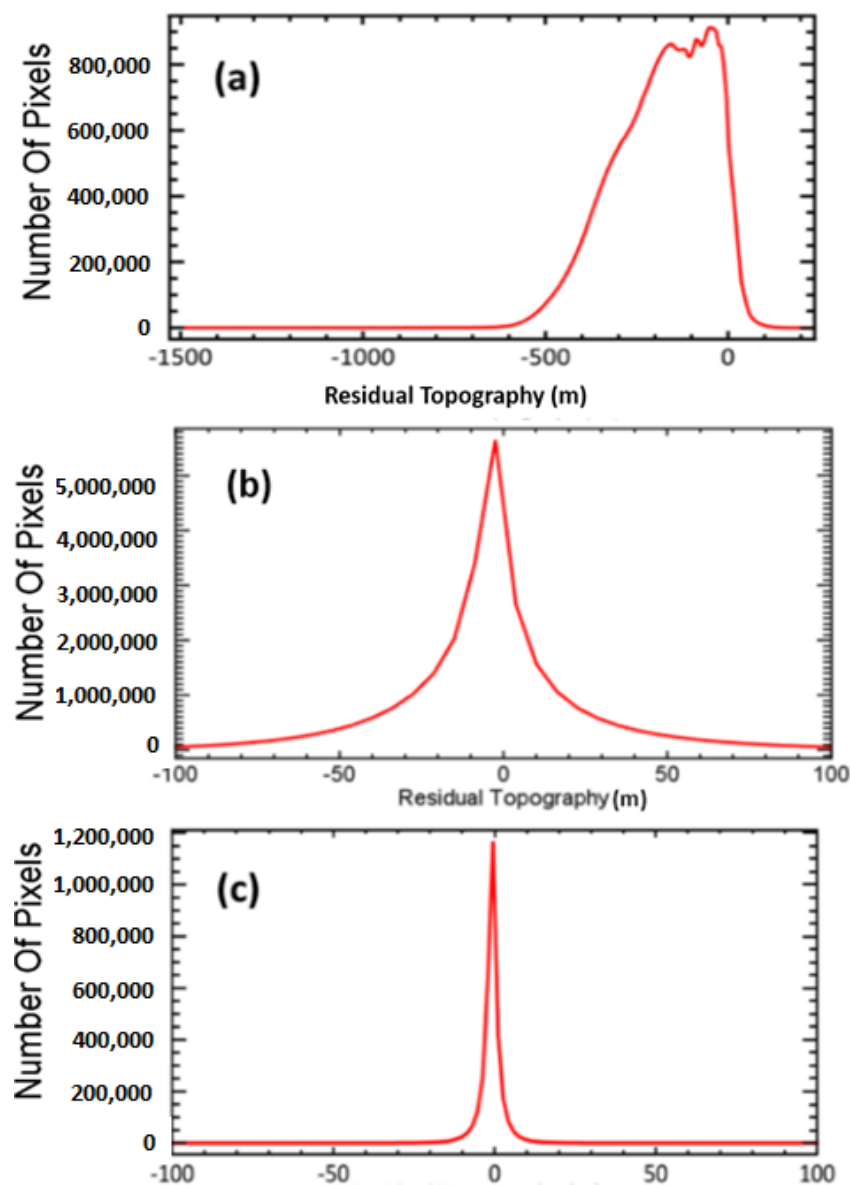
Figure 8. Statistics of estimated residual topography: (**a**) for ALOS-2 interferograms by using the SRTM data, which showed average residual topography equal to -100 m and high standard deviation equal to 70 m; (**b**) the average residual topography and standard deviation reduced by increasing the wavelet number; (**c**) for Sentinel-1 interferogram with average residual topography to almost 0 m with a standard deviation equal to 13.5 m.

Increasing the value of the wavelet to two means that the information that is coarser than 200 m is removed, while the information, which is finer than 200, is preserved. Such a result is highly unlikely because the estimation produced is extremely imprecise. It is clear that even after using a large wavelet number with the ALOS-2 SAR data, the Sentinel-1 interferograms with a zero wavelet showed an accurate and improved estimation of the average residual topography. After removing the residual topography, the phase information characterizes the displacement along the line of sight (LOS) direction. The sensitivity of displacement rate depends on the system wavelength. Thus, sensors with longer wavelength will have a sensitivity smaller than the sensors with a shorter wavelength.

Finally, all the obtained results were geocoded to adopt two constraints: the velocity and height precisions thresholds. To estimate meaningful thresholds, in terms of coverage and precision, the statistic tool of the ArcGIS was used (Figure 9). Consequently, the velocity precision threshold value of 9 mm/year and the height precision threshold value

of 35 m were used for Sentinel-1 data, while the velocity precision threshold value used for ALOS-2 data was 40 mm/year and the height precision threshold of 100 m.
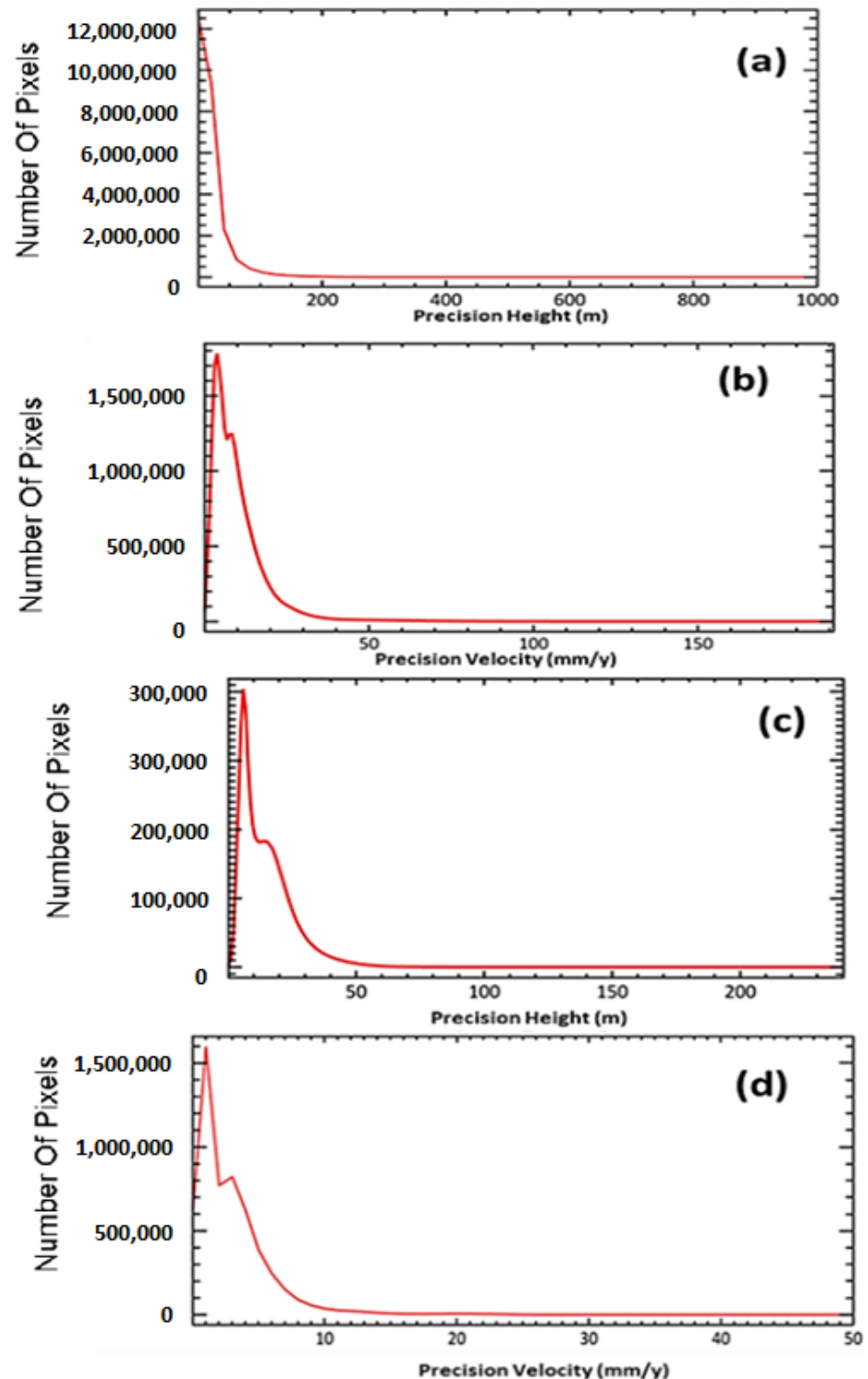

Figure 9. (**a**) Statistics histograms of precision height and (**b**) the corresponding height precision for ALOS/PALSAR-2 data. (**c**) Representative histograms of Sentinel-1 data precision height and (**d**) the corresponding precision velocity.

The deformation component can be isolated from the non-deformation component by addressing phase noise due to changing the properties of scattering over time. This has

been achieved by using the phase behavior of radar signals to select pixels with minimal decorrelation [75]. Thus, the accuracy of the final results depends on the final coherence and the wavelength of the used data. Accordingly, coherence of 0.2 in C-band comparable to a coherence of about 0.6 in L-band to obtain the same precision, but with less pixels. The final coherence result of Sentinel-1 data ranges from 0.2 to 0.75 with an average coherence value of about 0.4 and standard deviation of 0.11. Coherent pixels represent good coverage of all urban area of Alexandria City, which has been used in calculating the land subsidence (Figure 10). However, the final coherence coverage of ALOS-2 data is very poor with an average coherence value of about 0.6 and standard deviation of 0.04 and about 80% of Alexandria City showed no coherent data (Figure 11).
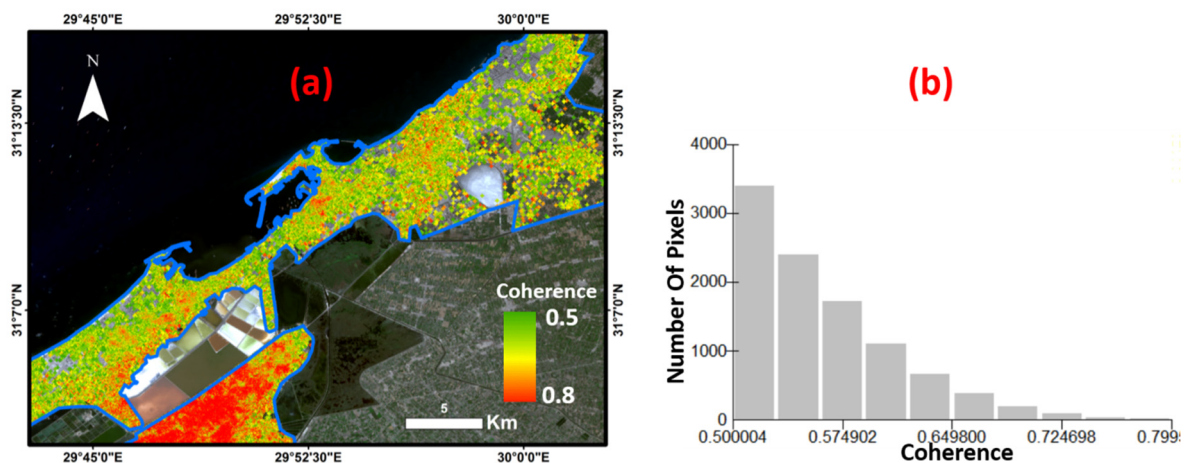

Figure 10. An excellent final coherence map result is shown based on the C-band Sentinel-1 data with values ranging from 0.5 to 0.8 (**a**) and its associated histogram (**b**).
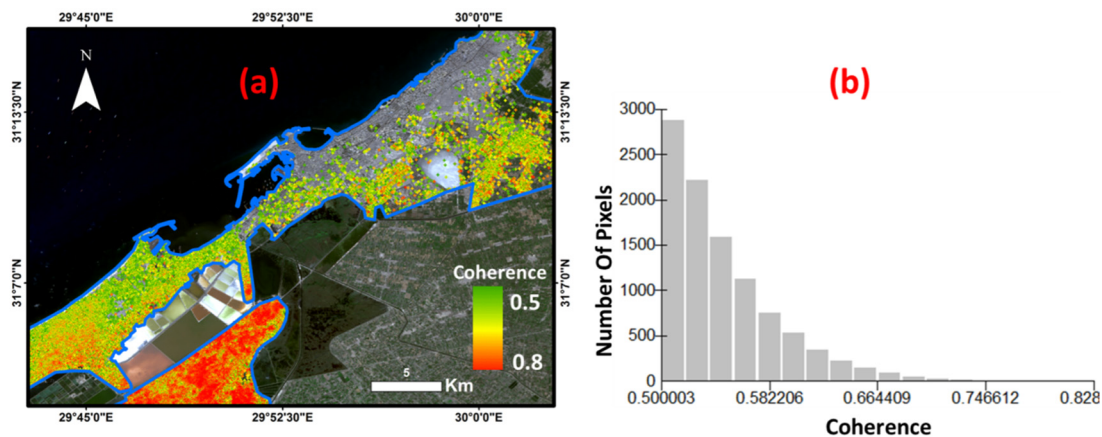

Figure 11. The final coherence coverage of ALOS-2 data which is very poor with average coherence values of about 0.6, standard deviation of 0.04 and about 80% of Alexandria City show no coherent data (**a**) and its associated histogram (**b**).

The measured average vertical displacement of Alexandria City during the period from 2015 to 2019 using a coherence threshold value of 0.2 for ALOS/PALSAR-2 data is about 5 cm for the maximum uplift rate and about −15 cm for the maximum vertical subsidence rate (Figure 12). Since ALOS-2 data do not have enough coherent pixels to be used to estimate the deformation along the urban areas, the final deformation results are discussed by using Sentinel-1 data with a threshold value of 0.4, which corresponds to a threshold value of 0.8 using ALOS-2 data.
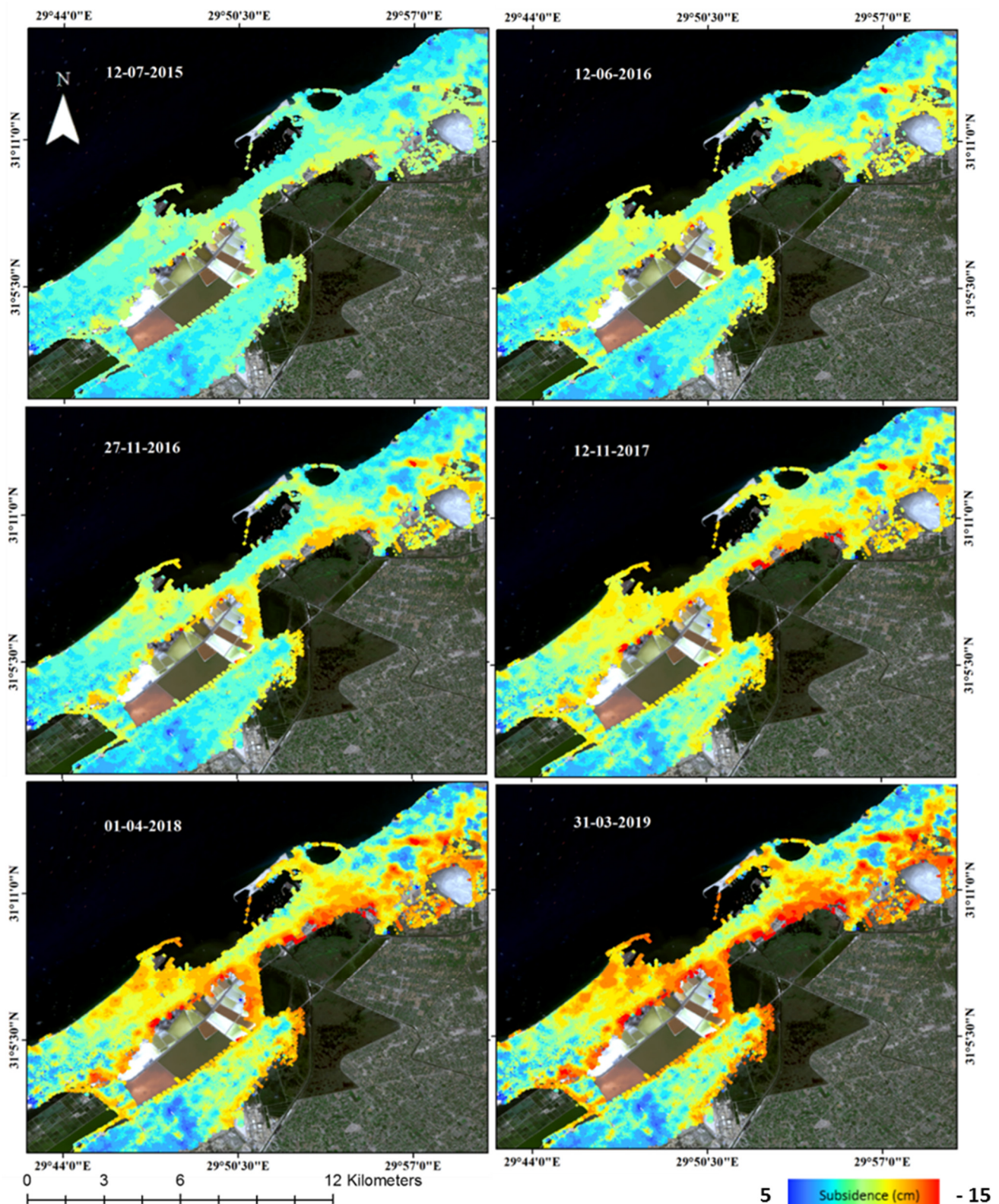
Figure 12. Vertical displacement of Alexandria City using coherence threshold value of 0.2 during the period from 2015 to 2019 using ALOS/PALSAR-2 images.

The deformation in the vertical direction along the study area can be clearly observed in Figure 13 during the period from 2017 to 2020. The color ramp from red to blue indicates the negative to positive velocities in the vertical direction. The negative values indicate the

surface is moving away from the satellite (subsidence), while the positive values indicate the opposite direction of movement (uplift). Vertical deformation from 2017 to 2018 varies between −30 mm and 20 mm (Figure 13a) with an average of −4 mm. Figure 13c,d presents the vertical motion from 2017 to 2019, which ranged between −40 mm and 20 mm with an average about −4.3 mm with a standard deviation of 8 mm. The cumulative displacement in vertical direction along the study area from 2017 to 2020 reached −60 mm away from the sensor with an average of −12.5 mm and standard deviation of −10 mm (Figure 13e,f). These calculated subsidence rates show the subsidence rate is not constant over the years.
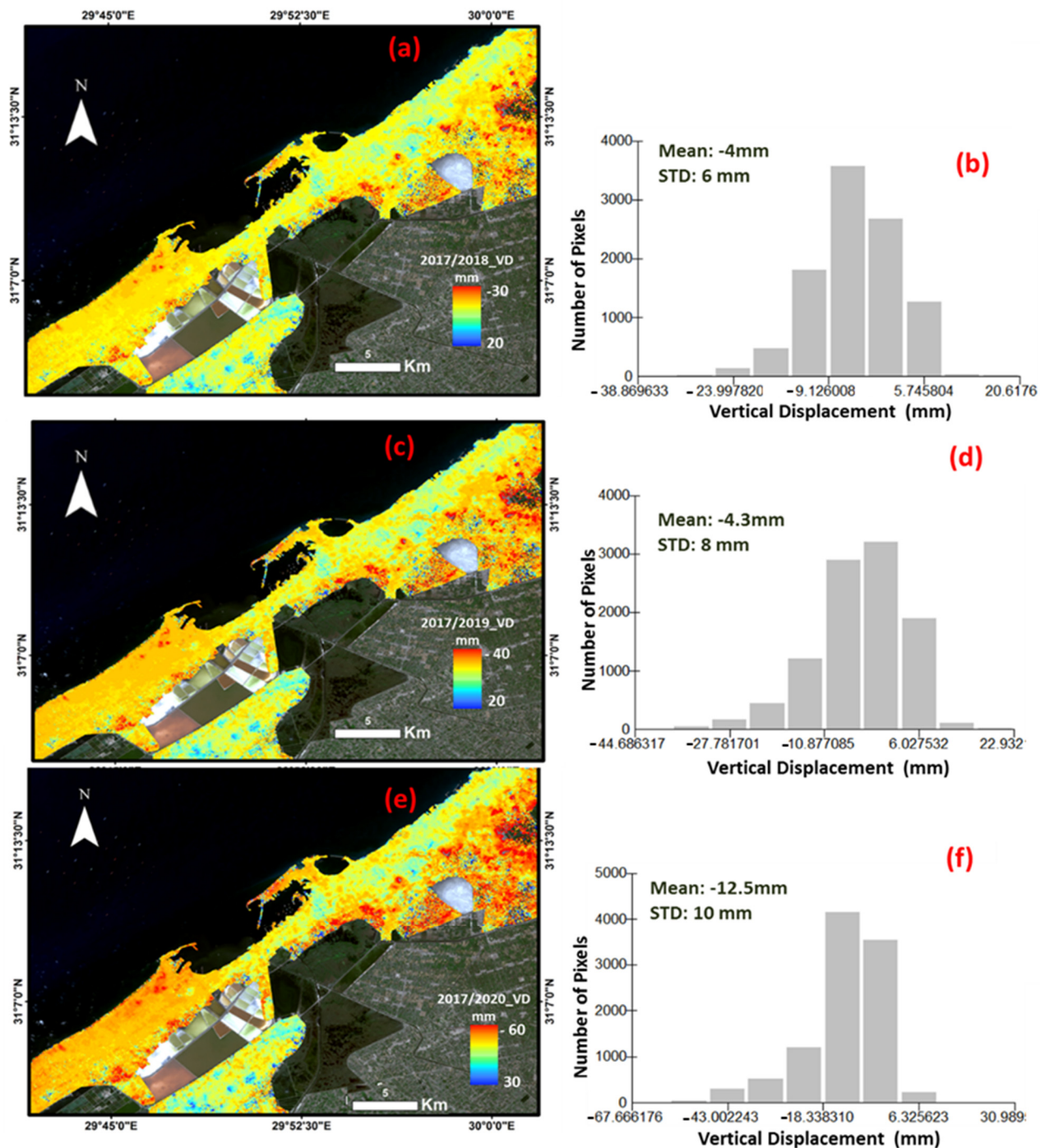

Figure 13. Vertical displacement of Alexandria City from: (**a**) 2017/2018; (**c**) 2017/2019; (**e**) 2017/2020 and the corresponding histograms of each period (**b**,**d**,**f**).

The mean velocity (mm/year) maps of the final geocoded vertical displacements generated from the Sentinel-1 data are shown in Figure 14. The histograms of the estimated displacement velocities along the study area are shown in Figure 14b, with an average displacement rate and a standard deviation of −1.73 and 4 mm/year, respectively.
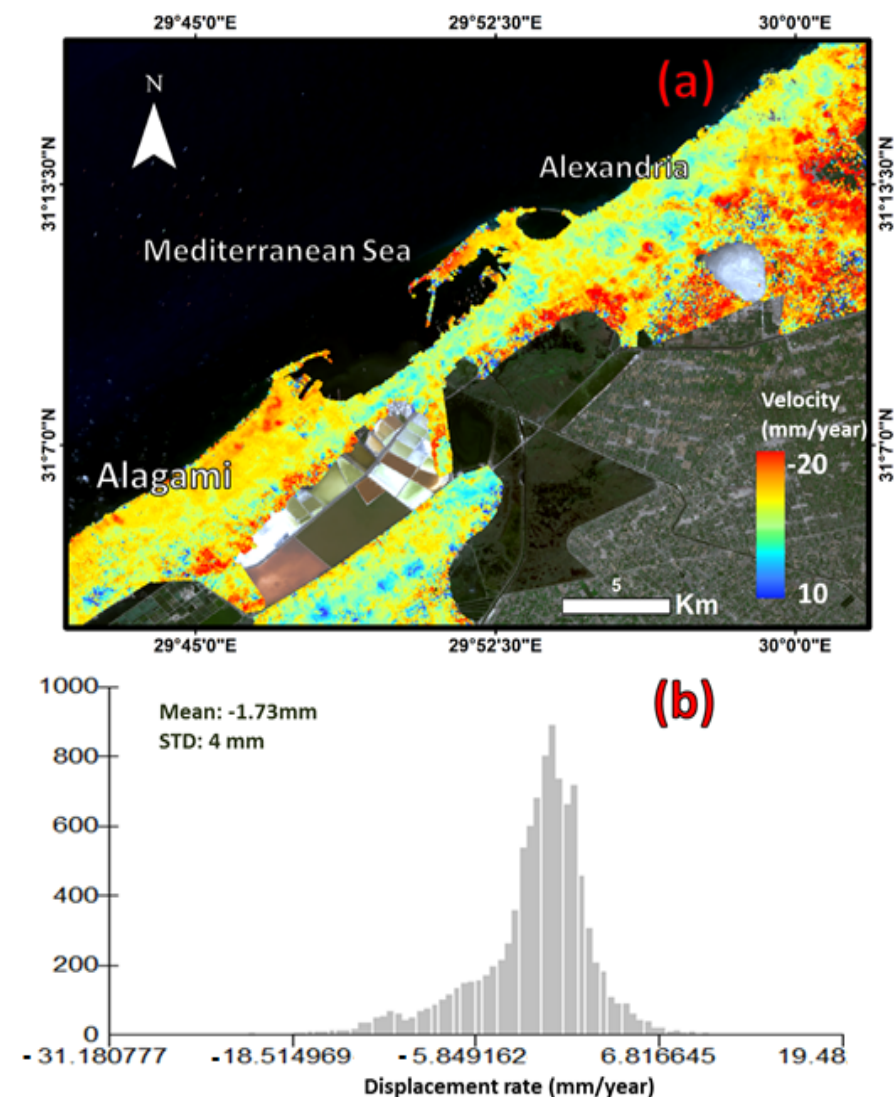

Figure 14. (**a**) The estimated mean displacement velocity of Alexandria and Alagami Cities using the Sentinel-1 data from August 2017 to September 2020 with coherence threshold of 0.4; (**b**) the corresponding histogram distribution of the derived displacement velocity rates.

6. Discussion

Selecting the proper master and slave SAR images with acceptable perpendicular and temporal baselines is a very important issue to avoid generating noisy interfeorograms. Such a selection should also consider the types of the surface features along the study area, where the urban areas can maintain a large temporal baseline, unlike the vegetation cover. Moreover, the coherence threshold value should be determined in a professional way so that a large number of pixels is used in order to achive high coherence with no surface changes and good matching between the different images.

All phase jumps, phase ramps, orbital inaccuracies, atmospheric artifacts and residual topography were calibrated and corrected before estimating the final vertical displacement to improve the accuracy of the results. The longer wavelength of SAR data shows less sensitivity, as well as less spatial coverage in calculating the land subsidence.

However, Alexandria is located at the western margin of the Nile Delta on a cemented Pleistocene sandstone ridge covered by a thin layer of Holocene sediments [76], except in the paleo island of Pharos and the former southern wetlands. Accordingly, the Alexandrian coastal plain and city center are considered to be relatively stable, with an estimated land subsidence of 0 to −5 mm/year. The maximum average subsidence value reached −20 mm/year, where the high subsidence areas are located mostly in the former Abu Qir Lagoon, the dry and recently reclaimed region of the former Mariout Lake, and parts of the northeast Alagami area.

The port of Alexandria plays an important role in Egypt's economy. Its capacity represents 75% of Egypt's total capacity Ports of the Mediterranean. It accounts for 40% of Egypt's total population industry and 56% of the petroleum industry. Due to new urbanized areas and infrastructure constructed for all of these facilities it has negatively affected the land deformation of Alexandria City. Whereas the city area constructed before 1917 was relatively stable relative to urban expansion. The city has been expanding more than double, mainly along its built-up areas during the last quarter century.

The type of Alexandria substrate rocks has an effect on the surface deformation. The soil substrate of Alexandria City represents carbon ridges, gravel, sand, stabilized sand dunes, oolitic beach and beach ridge, Nile silt and sabkha deposits, as well as refilled materials of the former lagoons. The maximum thickness of sabkha deposits reaches about 35 m in the south-western part of Alexandria where it plays an important role in accelerating the land subsidence compared to other lithological formations. The thickness of the Nile silt is about 30 m in the eastern and central part of the city. All pixels with velocity of less than −20 mm/year represent areas with different degrees of subsidence, as shown in the small-data-frame of Figure 14. Subsided areas were mainly distributed in the southern newly urbanized areas of the city, built on dried grounds from former lakes and lagoons (Figure 15).
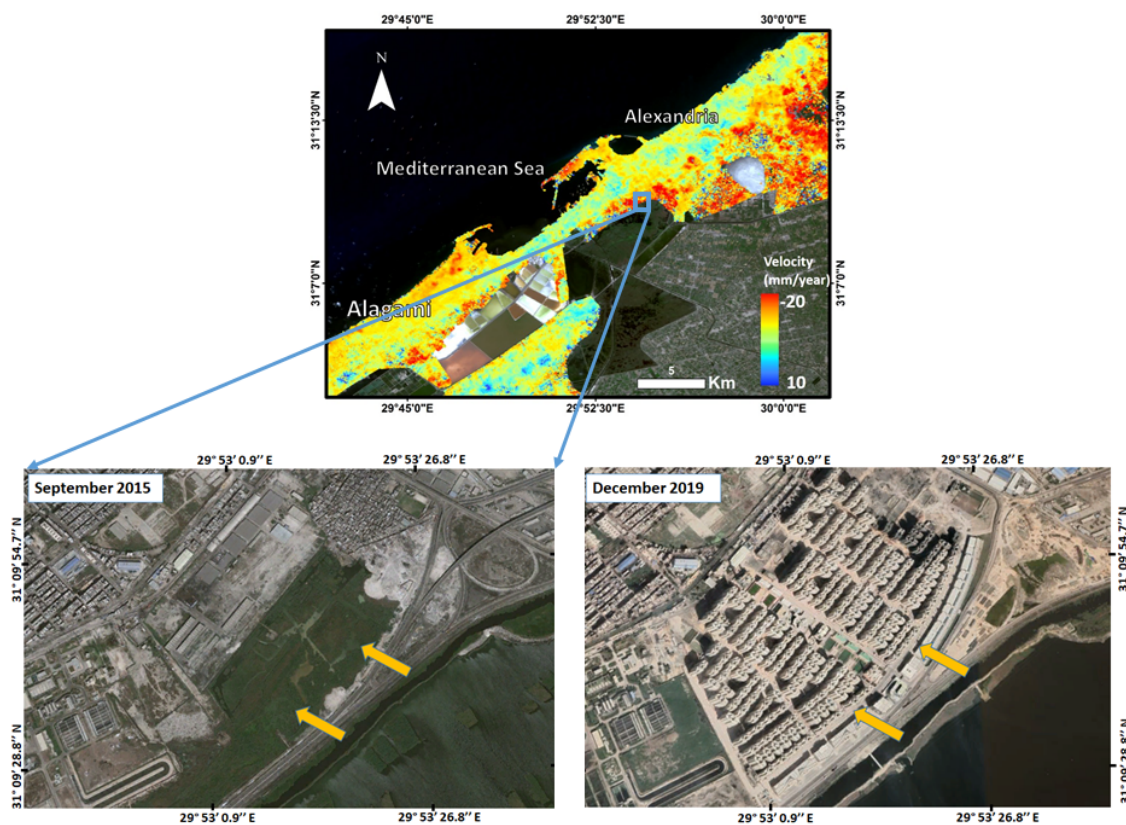

Figure 15. Shows the recent urban expansions along the border of former Mariout Lake causing land subsidence.

Subsidence are found in parts of the northwest (Alagami), newly reclaimed areas in the northeast of palaeo-island of Farous, the sandy tombolo of the old city, some parts of stabilized sand dunes in the eastern part of the city, and newly reclaimed areas in the far eastern side of Abu-Qir area. These subsidence areas are controlled by the subsurface rock type. There are three refilled and reclaimed areas from former lagoons, including the former Alharda Lake, a part of the former Abu-Qir Lagoon and a part of the former Mariout Lake in the south Western section of the study area (Figure 16). The dried and reclaimed areas from Abu-Qir Lagoon in the southeast of the study area have the highest average subsidence when compared to other dried and reclaimed former lakes and lagoon areas, about −20 mm/year. The reclaimed areas of the former Lake Alhadra showed the lowest annual average subsidence among dried and reclaimed former lakes and lagoon areas, −8.5 mm/year. Land subsidence was recorded in the refilled areas from a former lagoon in the southern part of the study area.
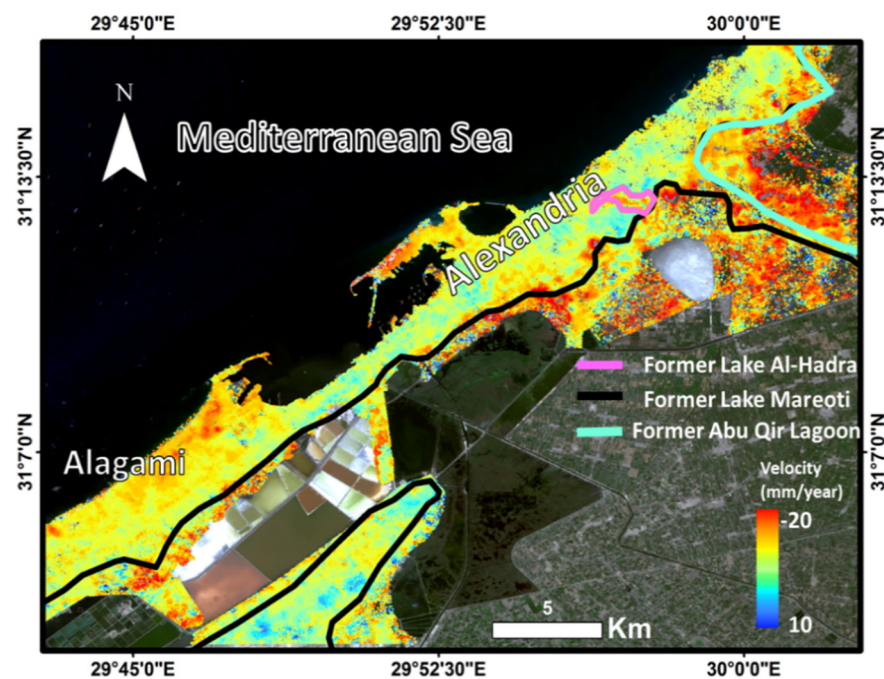

Figure 16. Former lakes and lagoons in Alexandria based on displacement velocity of Alexandria and Alagami cities using the Sentinel-1 data from August 2017 to September 2020.

Different levels of subsidence at different locations along the study area leave visual marks on the surface of the city. The field investigation provided supporting evidence of the results presented in this study. Figure 17 shows the visual cracks on buildings and roads captured at subsided locations, as defined in our vertical displacement results. Different degrees of subsidence can be easily inferred from the road cracks shown in the pictures in Figure 17b–d. The subsidence and field-checked buildings were plotted on the final land subsidence maps derived from Sentinel-1 data using the SBAS technique. The location of the affected buildings shows high consistency with the estimated results of the DInSAR.

The frequently occurred land subsidence events along the Alexandria City, especially along the newly urbanized areas should be carefully considered for future expansion or any other developmental plans. This is to avoid any related hazards that might cause damages. The western desert fringes of Alexandria should be considered for future developmental plans instead of the southern part of the city, which is suffering from the high subsidence rate due to its fragile substrate soil.
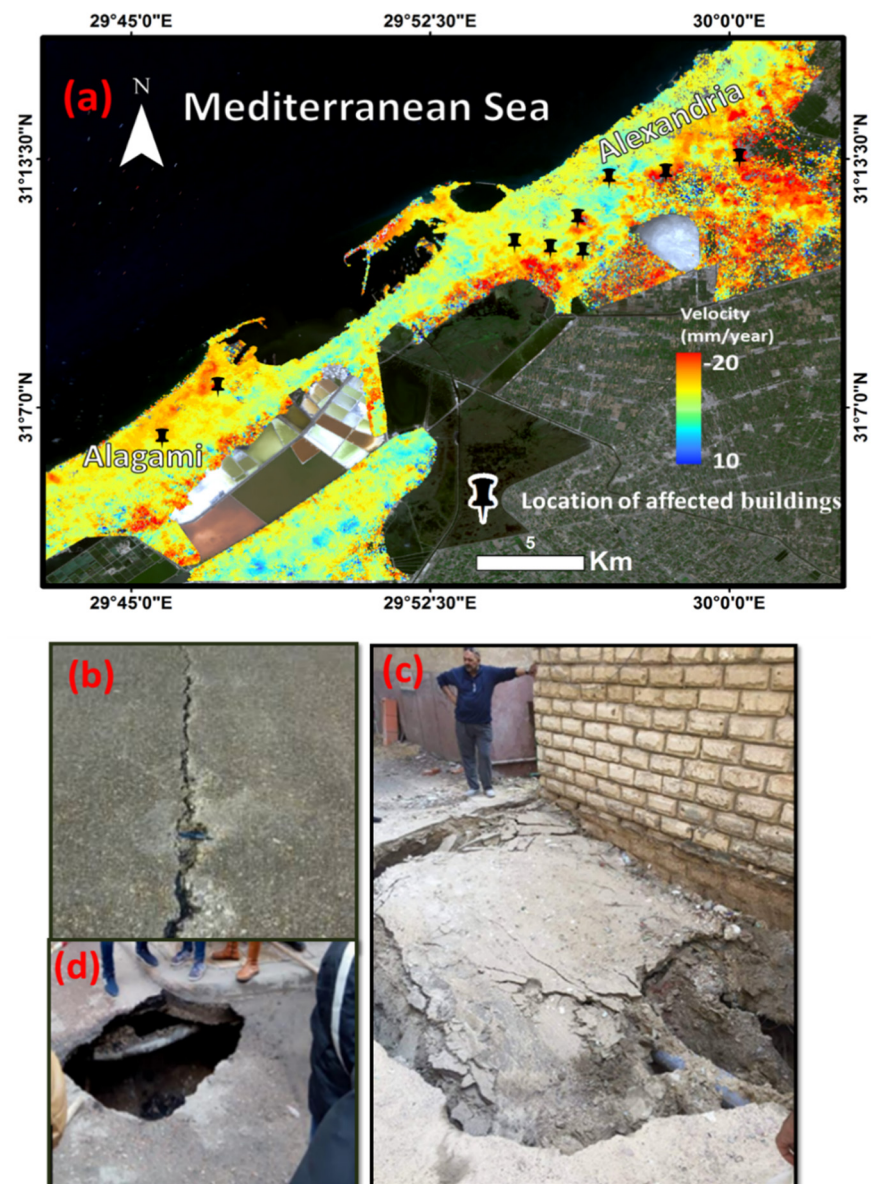
Figure 17. Land-Subsidence map shows the locations of the affected buildings (**a**); samples of cracks on roads and ground deformations located in high subsided areas (**b**–**d**).

7. Conclusions

Quantifying the vertical land displacement with high accuracy is a very important aspect in many applied science fields, especially those focusing on mitigating the resulting environmental hazards and their impact on various human driven activities and infrastructure. Meanwhile, the DInSAR is considered as one of the best tools to provide such deformation measures with very high accuracy and with good spatial coverage. In this study, different SAR sensors (Sentinel-1 and ALOS/PALSAR-2) were used to assess their relative accuracy in estimating the land subsidence along the coastal city of Alexandria in Egypt, which was selected as a test site. A total of nine Sentinel-1 and 11 ALOS/PALSAR-2 data covering the period of 2017 to 2020 were processed using the SBAS method approach.

The Sentinel-1 C-band data showed higher coherence and less residual topography than the ALOS/PALSAR-2 L-band. Consequently, there are not enough distributed coherent pixels in the ALOS-2 data to be used to accurately represent the deformation for urban along the study area, thus the final deformation result was discussed by using Sentinel-1 data only. The cumulative displacement pattern in vertical direction from 2017 to 2020

recorded −60 mm away from the sensor with an average of −12.5 mm and a standard deviation of −10 mm. These results show that the Alexandria coastal plain and main city center are considered to be relatively stable, with estimates of 0 to −5 mm/year. However, the maximum average subsidence value was estimated as −20 mm/year and located mostly along the dried regions of the former Abu Qir Lagoon and Mariout Lake, as well as parts of the northeast Alagami area. Finally, the results have been validated using field information, which show good correlation. In addition, the western desert fringes of Alexandria should be considered for future developmental plans instead of the southern part, which show a high subsidence rate due to its fragile substrate soil.

References

1. Frihy, O.E. Some proposals for coastal management of the Nile delta coast. *Ocean Coast. Manag.* **1996**, *30*, 43–59. [CrossRef]
2. Warne, A.G.; Stanley, J.D. Late Quaternary evolution of the northwest Nile delta and adjacent coast in the Al-exandria region, Egypt. *J. Coast. Res.* **1993**, *9*, 26–64.
3. Stanley, D.J.; Warne, A.G. Nile Delta in its destruction phase. *J. Coast. Res.* **1998**, *14*, 795–825.
4. Bridge, J.S. *Rivers and Floodplains: Forms, Processes, and Sedimentary Record*; John Wiley & Sons: Hoboken, NJ, USA, 2009.
5. Lu, Z.; Kwoun, O.-I. Radarsat-1 and ERS InSAR Analysis Over Southeastern Coastal Louisiana: Implications for Mapping Water-Level Changes Beneath Swamp Forests. *IEEE Trans. Geosci. Remote Sens.* **2008**, *46*, 2167–2184. [CrossRef]
6. Jiang, L.; Lin, H.; Cheng, S. Monitoring and assessing reclamation settlement in coastal areas with advanced InSAR techniques: Macao city (China) case study. *Int. J. Remote Sens.* **2011**, *32*, 3565–3588. [CrossRef]
7. Liu, P. *InSAR Observations and Modeling of Earth Surface Displacements in the Yellow River Delta (China)*; University of Glasgow: Glasgow, UK, 2012.
8. Wang, H.; Wright, T.J.; Yu, Y.; Lin, H.; Jiang, L.; Li, C.; Qiu, G. InSAR reveals coastal subsidence in the Pearl River Delta, China. *Geophys. J. Int.* **2012**, *191*, 1119–1128. [CrossRef]
9. Oliver-Cabrera, T.; Wdowinski, S. InSAR-based mapping of tidal inundation extent and amplitude in Louisiana coastal wetlands. *Remote Sens.* **2016**, *8*, 393. [CrossRef]
10. Zhang, B.; Wdowinski, S.; Oliver-Cabrera, T.; Koirala, R.; Jo, M.J.; Osmanoglu, B. Mapping the Extent and Magnitude of Sever Flooding Induced by Hurricane Irma with Multi-Temporal Sentinel-1 Sar and Insar Observations. *ISPRS Int. Arch. Photogramm. Remote Sens. Spat. Inf. Sci.* **2018**, *3*, 2237–2244. [CrossRef]
11. Zhao, Q.; Ma, G.; Wang, Q.; Yang, T.; Liu, M.; Gao, W.; Falabella, F.; Mastro, P.; Pepe, A. Generation of long-term InSAR ground displacement time-series through a novel multi-sensor data merging technique: The case study of the Shanghai coastal area. *ISPRS J. Photogramm. Remote Sens.* **2019**, *154*, 10–27. [CrossRef]
12. Aly, M.H. Radar Interferometry for Monitoring Land Subsidence and Coastal Change in the Nile Delta, Egypt. Ph.D. Thesis, Texas A&M University, College Station, TX, USA, 2006.
13. Becker, R.H.; Sultan, M. Land subsidence in the Nile Delta: Inferences from radar interferometry. *Holocene* **2009**, *19*, 949–954. [CrossRef]
14. Hereher, M.E. Vulnerability of the Nile Delta to sea level rise: An assessment using remote sensing. *Geomat. Nat. Hazards Risk* **2010**, *1*, 315–321. [CrossRef]
15. El-Asmar, H.M.; Hereher, M.E. Change detection of the coastal zone east of the Nile Delta using remote sensing. *Environ. Earth Sci.* **2010**, *62*, 769–777. [CrossRef]
16. Aly, M.H.; Klein, A.G.; Zebker, H.A.; Giardino, J.R. Land subsidence in the Nile Delta of Egypt observed by persistent scatterer interferometry. *Remote Sens. Lett.* **2012**, *3*, 621–630. [CrossRef]
17. Bouali, E.; Sultan, M.; Becker, R.; Cherif, O. *Using Persistent Scatterers Interferometry to Create a Subsidence Map of the Nile Delta in Egypt*; American Geophysical Union: Washington, DC, USA, 2013.
18. Hassaan, M.A.; Abdrabo, M.A. Vulnerability of the Nile Delta coastal areas to inundation by sea level rise. *Environ. Monit. Assess.* **2012**, *185*, 6607–6616. [CrossRef] [PubMed]
19. Fugate, J.M. Measurements of Land Subsidence Rates on the North-Western Portion of the Nile Delta Using Radar Interferometry Techniques. Ph.D. Thesis, University of Toledo, Toledo, OH, USA, 2014.

20. Gaber, A.; Darwish, N.; Sultan, Y.; Arafat, S.; Koch, M. Monitoring Building Stability in Port-Said City, Egypt Using Differential SAR Interferometry. *Int. J. Environ. Sustain.* **2014**, *3*. [CrossRef]

21. Gaber, A.; Darwish, N.; Koch, M. Minimizing the Residual Topography Effect on Interferograms to Improve DInSAR Results: Estimating Land Subsidence in Port-Said City, Egypt. *Remote Sens.* **2017**, *9*, 752. [CrossRef]

22. Stanley, J.-D.; Clemente, P.L. Increased Land Subsidence and Sea-Level Rise Are Submerging Egypt's Nile Delta Coastal Margin. *GSA Today* **2017**, *27*, 4–11. [CrossRef]

23. Gebremichael, E.; Sultan, M.; Becker, R.; El Bastawesy, M.; Cherif, O.; Emil, M. Assessing Land Deformation and Sea Encroachment in the Nile Delta: A Radar Interferometric and Inundation Modeling Approach. *J. Geophys. Res. Solid Earth* **2018**, *123*, 3208–3224. [CrossRef]

24. Sataer, G.; Sultan, M.; Emil, M.K.; Palaseanu, M.; Becker, R.; Kehew, A.; Yellich, J.A.; Kincare, K. *Visualizing and Monitoring Bluff Retreat Using Sentinel 1 Radar Interferometry and UAV Imagery*; American Geophysical Union: Washington, DC, USA, 2019.

25. Rateb, A.; Abotalib, A.Z. Inferencing the land subsidence in the Nile Delta using Sentinel-1 satellites and GPS between 2015 and 2019. *Sci. Total. Environ.* **2020**, *729*, 138868. [CrossRef]

26. Williams, J.G.; Rosser, N.J.; Kincey, M.E.; Benjamin, J.; Oven, K.J.; Densmore, A.L.; Milledge, D.G.; Robinson, T.R.; Jordan, C.A.; Dijkstra, T.A. Satellite-based emergency mapping using optical imagery: Experience and reflections from the 2015 Nepal earthquakes. *Nat. Hazards Earth Syst. Sci.* **2018**, *18*, 185–205. [CrossRef]

27. Kargel, J.S.; Leonard, G.J.; Shugar, D.H.; Haritashya, U.K.; Bevington, A.; Fielding, E.J.; Fujita, K.; Geertsema, M.; Miles, E.S.; Steiner, J.; et al. Geomorphic and geologic controls of geohazards induced by Nepals 2015 Gorkha earthquake. *Science* **2015**, *351*, aac8353. [CrossRef] [PubMed]

28. Bessette-Kirton, E.K.; Cerovski-Darriau, C.; Schulz, W.H.; Coe, J.A.; Kean, J.W.; Godt, J.W.; Thomas, M.A.; Hughes, K.S. Landslides triggered by Hurricane Maria: Assessment of an extreme event in Puerto Rico. *GSA Today* **2019**, *29*, 4–10.

29. Robinson, T.R.; Rosser, N.; Walters, R.J. The Spatial and Temporal Influence of Cloud Cover on Satellite-Based Emergency Mapping of Earthquake Disasters. *Sci. Rep.* **2019**, *9*, 12455–12459. [CrossRef] [PubMed]

30. Dai, K.; Li, Z.; Tomás, R.; Liu, G.; Yu, B.; Wang, X.; Cheng, H.; Chen, J.; Stockamp, J. Monitoring activity at the Daguangbao mega-landslide (China) using Sentinel-1 TOPS time series interferometry. *Remote Sens. Environ.* **2016**, *186*, 501–513. [CrossRef]

31. Bonì, R.; Bordoni, M.; Colombo, A.; Lanteri, L.; Meisina, C. Landslide state of activity maps by combining multi-temporal A-DInSAR (LAMBDA). *Remote Sens. Environ.* **2018**, *217*, 172–190. [CrossRef]

32. Handwerger, A.L.; Fielding, E.J.; Huang, M.; Bennett, G.L.; Liang, C.; Schulz, W.H. Widespread Initiation, Reactivation, and Acceleration of Landslides in the Northern California Coast Ranges due to Extreme Rainfall. *J. Geophys. Res. Earth Surf.* **2019**, *124*, 1782–1797. [CrossRef]

33. Hu, X.; Bürgmann, R.; Lu, Z.; Handwerger, A.L.; Wang, T.; Miao, R. Mobility, Thickness, and Hydraulic Diffusivity of the Slow-Moving Monroe Landslide in California Revealed by L-Band Satellite Radar Interferometry. *J. Geophys. Res. Solid Earth* **2019**, *124*, 7504–7518. [CrossRef]

34. Aslan, G.; Foumelis, M.; Raucoules, D.; De Michele, M.; Bernardie, S.; Cakir, Z. Landslide Mapping and Monitoring Using Persistent Scatterer Interferometry (PSI) Technique in the French Alps. *Remote Sens.* **2020**, *12*, 1305. [CrossRef]

35. Bekaert, D.P.; Handwerger, A.L.; Agram, P.; Kirschbaum, D.B. InSAR-based detection method for mapping and monitoring slow-moving landslides in remote regions with steep and mountainous terrain: An application to Nepal. *Remote Sens. Environ.* **2020**, *249*, 111983. [CrossRef]

36. Reyes-Carmona, C.; Barra, A.; Galve, J.P.; Monserrat, O.; Pérez-Peña, J.V.; Mateos, R.M.; Notti, D.; Ruano, P.; Millares, A.; López-Vinielles, J. Sentinel-1 DInSAR for Monitoring Active Landslides in Critical Infrastructures: The Case of the Rules Reservoir (Southern Spain). *Remote Sens.* **2020**, *12*, 809. [CrossRef]

37. Solari, L.; Del Soldato, M.; Raspini, F.; Barra, A.; Bianchini, S.; Confuorto, P.; Casagli, N.; Crosetto, M. Review of Satellite Interferometry for Landslide Detection in Italy. *Remote Sens.* **2020**, *12*, 1351. [CrossRef]

38. Bitelli, G.; Bonsignore, F.; Carbognin, L.; Ferretti, A.; Strozzi, T.; Teatini, P.; Tosi, L.; Vittuari, L. Radar interferome-try-based mapping of the present land subsidence along the low-lying northern Adriatic coast of Italy. Land Subsidence, Associated Hazards and the Role of Natural Resources Development. In Proceedings of the EISOLS 2010, Queretaro, Mexico, 17–22 October 2010; pp. 279–286.

39. Ruiz, A.M.; Caro, M.; Sousa, J.J.; Gil, A.J.; Hanssen, R.F.; Perski, Z.; Galindo-Zaldívar, J.; de Galdeano, C.S. Land subsidence monitoring in the southern Spanish coast using satellite radar interferometry. *Sci. Total Environ. J.* **2018**, *636*, 670–687. [CrossRef]

40. De Macedo, K.A.C.; Ramos, F.L.G.; Gaboardi, C.; Moreira, J.R.; Vissirini, F.; Da Costa, M.S. A Compact Ground-Based Interfero-metric Radar for Landslide Monitoring: The Xerém Experiment. *IEEE J. Sel. Top. Appl. Earth Obs. Remote Sens.* **2017**, *10*, 975–986. [CrossRef]

41. Ruiz-Armenteros, A.M.; Lazecky, M.; Ruiz-Constán, A.; Bakoň, M.; Delgado, J.M.; Sousa, J.J.; Galindo-Zaldívar, J.; de Galdeano, C.S.; Caro-Cuenca, M.; Martos-Rosillo, S. Monitoring continuous subsidence in the Costa del Sol (Málaga province, southern Spanish coast) using ERS-1/2, Envisat, and Sentinel-1A/B SAR interferometry. *Procedia Comput. Sci.* **2018**, *138*, 354–361. [CrossRef]

42. Achache, J.; Fruneau, B.; Delacourt, C. Applicability of SAR interferometry for monitoring of landslides. In Proceedings of the ERS Applications Workshop, London, UK, 6–8 December 1995.

43. Fruneau, B.; Achache, J.; Delacourt, C. Observation and modelling of the Saint-Étienne-de-Tinée landslide using SAR interferome-try. *Tectonophysics* **1996**, *265*, 181–190. [CrossRef]

44. Vietmeier, J.W.; Wagner, W.; Dikau, R. Monitoring moderate slope movements (landslides) in the southern French Alps using differential SAR interferometry. In Proceedings of the Second International Workshop on ERS SAR Interferometry, FRINGE'99, Liège, Belgium, 10−12 November 1999.

45. Rizo, V.; Tesauro, M. SAR interferometry and field data of Randazzo landslide (Eastern Sicily, Italy). *Phys. Chem. Earth Part B Hydrol. Oceans Atmos.* **2000**, *25*, 771–780. [CrossRef]

46. Squarzoni, C.; Delacourt, C.; Allemand, P. Nine years of spatial and temporal evolution of the La Valette landslide observed by SAR interferometry. *Eng. Geol.* **2003**, *68*, 53–66. [CrossRef]

47. Ferretti, A.; Prati, C.; Rocca, F. Permanent scatterers in SAR interferometry. *IEEE Trans. Geosci. Remote Sens.* **2001**, *39*, 8–20. [CrossRef]

48. Berardino, P.; Fornaro, G.; Lanari, R.; Sansosti, E. A new algorithm for surface deformation monitoring based on small baseline differential SAR interferograms. *IEEE Trans. Geosci. Remote Sens.* **2002**, *40*, 2375–2383. [CrossRef]

49. Mohamed, A. A Decision from the Governor of Alexandria Regarding Land Subsidence and the Neighborhood: The Geb Factory. *Egypt News.* Available online: https://www.eg24.news (accessed on 28 March 2021).

50. Agrawala, S.; Moehner, A.; El Raey, M.; Conway, D.; Van Aalst, M.; Hagenstad, M.; Smith, J. Development and climate change in Egypt: Focus on coastal resources and the Nile. *Organ. Econ. Coop. Dev.* **2004**, *1*, 1–68.

51. El-Raey, M. Impacts and implications of climate change for the coastal zones of Egypt. In *Coastal Zones and Climate Change*; The Henry L. Stimson Center: Washington, DC, USA, 2010; pp. 31–49, ISBN 978-0-9821935-5-6.

52. Sampsell, B.M.; van Hasselt, B. *Geology of Egypt*; The American University in Cairo Press: Cairo, Egypt, 2003.

53. Said, R. *The Geological Evolution of the River Nile*; Springer: Berlin/Heidelberg, Germany, 1981.

54. Stanley, J.-D.; Clemente, P.L. Clay distributions, grain sizes, sediment thicknesses, and compaction rates to in-terpret subsidence in Egypt's northern Nile Delta. *J. Coast. Res.* **2014**, *30*, 88–101.

55. Stanley, J.-D. Growth faults, a distinct carbonate-siliciclastic interface and recent coastal evolution, NW Nile Delta, Egypt. *J. Coast. Res.* **2005**, *42*, 309–318.

56. Foumelis, M.; Blasco, J.M.D.; Desnos, Y.-L.; Engdahl, M.; Fernández, D.; Veci, L.; Lu, J.; Wong, C. ESA SNAP-StaMPS integrated processing for Sentinel-1 persistent scatterer interferometry. In Proceedings of the International Geoscience and Remote Sensing Symposium—IGARSS 2018, Valencia, Spain, 22–27 July 2018; pp. 1364–1367.

57. Wöppelmann, G.; Le Cozannet, G.; De Michele, M.; Raucoules, D.; Cazenave, A.; Garcin, M.; Hanson, S.; Marcos, M.; Santamaría-Gómez, A. Is land subsidence increasing the exposure to sea level rise in Alexandria, Egypt? *Geophys. Res. Lett.* **2013**, *40*, 2953–2957. [CrossRef]

58. Liosis, N.; Marpu, P.R.; Pavlopoulos, K.; Ouarda, T.B. Ground subsidence monitoring with SAR interferometry techniques in the rural area of Al Wagan, UAE. *Remote Sens. Environ.* **2018**, *216*, 276–288. [CrossRef]

59. Lanari, R.; Casu, F.; Manzo, M.; Zeni, G.; Berardino, P.; Manunta, M.; Pepe, A. An Overview of the Small Baseline Subset Algorithm: A DInSAR Technique for Surface Deformation Analysis. *Pure Appl. Geophys.* **2007**, *164*, 637–661. [CrossRef]

60. Diao, X.; Bai, Z.; Wu, K.; Zhou, D.; Li, Z. Assessment of mining-induced damage to structures using InSAR time series analysis: A case study of Jiulong Mine, China. *Environ. Earth Sci.* **2018**, *77*, 166. [CrossRef]

61. Hu, B. Monitoring of Ground Deformation due to Excessive Withdrawal of Natural Gas Using SBAS. *Math. Probl. Eng.* **2014**, *2014*, 1–6. [CrossRef]

62. Chaabani, A.; Deffontaines, B. Application of the SBAS-DInSAR technique for deformation monitoring in Tunis City and Mornag plain. *Geomat. Nat. Hazards Risk* **2020**, *11*, 1346–1377. [CrossRef]

63. Hooper, A. A multi-temporal InSAR method incorporating both persistent scatterer and small baseline approaches. *Geophys. Res. Lett.* **2008**, *35*, 302. [CrossRef]

64. Gierull, C. Statistical analysis of multilook SAR interferograms for CFAR detection of ground moving targets. *IEEE Trans. Geosci. Remote Sens.* **2004**, *42*, 691–701. [CrossRef]

65. Woodhouse, I.H. *Introduction to Microwave Remote Sensing*; CRC Press: Boca Raton, FL, USA, 2017.

66. Sarmap. PS Tutorial: Version 0.9. 2014. Available online: http://sarmap.ch/page.php?page=tutorials (accessed on 16 February 2016).

67. Gama, F.F.; Cantone, A.; Mura, J.C.; Pasquali, P.; Paradella, W.R.; dos Santos, A.R.; Silva, G.G. Monitoring subsidence of open pit iron mines at Carajás Province based on SBAS interferometric technique using TerraSAR-X data. *Remote Sens. Appl. Soc. Environ.* **2017**, *8*, 199–211. [CrossRef]

68. Zhang, Y.; Meng, X.; Jordan, C.; Novellino, A.; Dijkstra, T.; Chen, G. Investigating slow-moving landslides in the Zhouqu region of China using InSAR time series. *Landslides* **2018**, *15*, 1299–1315. [CrossRef]

69. Loesch, E.; Sagan, V. SBAS Analysis of Induced Ground Surface Deformation from Wastewater Injection in East Central Oklahoma, USA. *Remote Sens.* **2018**, *10*, 283. [CrossRef]

70. Ferretti, A.; Prati, C.; Rocca, F. Nonlinear subsidence rate estimation using permanent scatterers in differential SAR interferometry. *IEEE Trans. Geosci. Remote Sens.* **2000**, *38*, 2202–2212. [CrossRef]

71. Pendry, L.F.; Salvatore, J. Individual and social benefits of online discussion forums. *Comput. Hum. Behav.* **2015**, *50*, 211–220. [CrossRef]

72. Zebker, H.A.; Goldstein, R.M. Topographic mapping from interferometric synthetic aperture radar observations. *J. Geophys. Res. Solid Earth* **1986**, *91*, 4993–4999. [CrossRef]

73. Mora, O.; Lanari, R.; Mallorqui, J.J.; Berardino, P.; Sansosti, E. A new algorithm for monitoring localized deformation phenomena based on small baseline differential SAR interferograms. In Proceedings of the IEEE International Geoscience and Remote Sensing Symposium, Toronto, ON, Canada, 24–28 June 2002.
74. Rao, X.; Tang, Y. Small baseline subsets approach of DInSAR for investigating land surface deformation along the high-speed railway. In *SPIE Asia-Pacific Remote Sensing*; SPIE International Society for Optics and Photonics: Beijing, China, 2014; p. 92601C.
75. Bekaert, D.; Walters, R.; Wright, T.; Hooper, A.; Parker, D. Statistical comparison of InSAR tropospheric correction techniques. *Remote Sens. Environ.* **2015**, *170*, 40–47. [CrossRef]
76. Stanley, J.-D.; Toscano, M.A. Ancient archaeological sites buried and submerged along Egypt's Nile delta coast: Gauges of Holocene delta margin subsidence. *J. Coast. Res.* **2009**, *25*, 158–170. [CrossRef]